

Decay dynamics of the unbound ^{25}O and ^{26}O nuclei

K. Hagino^{1,2,3} and H. Sagawa^{4,5}

¹ *Department of Physics, Tohoku University, Sendai 980-8578, Japan*

² *Research Center for Electron Photon Science, Tohoku University, 1-2-1 Mikamine, Sendai 982-0826, Japan*

³ *National Astronomical Observatory of Japan, 2-21-1 Osawa, Mitaka, Tokyo 181-8588, Japan*

⁴ *RIKEN Nishina Center, Wako 351-0198, Japan*

⁵ *Center for Mathematics and Physics, University of Aizu, Aizu-Wakamatsu, Fukushima 965-8560, Japan*

We study the ground and excited resonance states of ^{26}O with a three-body model of $^{24}\text{O}+n+n$ taking into account the coupling to the continuum. To this end, we use the new experimental data for the invariant mass spectroscopy of the unbound ^{25}O and ^{26}O nuclei, and present an update of three-body model calculations for the two-neutron decay of the ^{26}O nucleus. With the new model inputs determined with the ground state decay of ^{26}O , we discuss the di-neutron correlations and a halo nature of this nucleus, as well as the structure of the excited states. For the energy of the 2^+ state, we achieve an excellent agreement with the experimental data with this calculation. We show that the 2^+ state consists predominantly of the $(d_{3/2})^2$ configuration, for which the pairing interaction between the valence neutrons slightly decreases its energy from the unperturbed one. We also discuss the structure of excited 0^+ states of the ^{26}O nucleus. In particular, we show the existence of an excited 0^+ state at 3.38 MeV, which is mainly composed of the $(f_{7/2})^2$ configuration.

PACS numbers: 21.10.-k, 21.10.Gv, 23.90.+w, 27.30.+t

I. INTRODUCTION

In recent years, there has been a rapidly increasing interest in two-neutron decays of unbound nuclei beyond the neutron drip line [1–22]. These are similar phenomena to the two-proton radioactivities in unbound nuclei beyond the proton-drip line [23], but with neutrons. While the resonance in proton radioactivity is mainly due to the Coulomb barrier, the resonant two-neutron emission arises from penetration of a centrifugal barrier. Since the long range Coulomb interaction is absent in the two-neutron decays, it has in general been expected that nucleon correlations, such as the dineutron correlations [24–28], are easier to be probed in the two-neutron decays as compared to the two-proton decays.

Among the two-neutron emitters studied so far, the ^{26}O nucleus has attracted a particular attention [11–15, 18–21], owing partly to the problem of abrupt termination of neutron-drip line for the oxygen isotopes at the neutron number $N=16$ [29, 30]. The ground state decay of this nucleus was first observed by Lunderberg *et al.* at the National Superconducting Cyclotron Laboratory (NSCL) at Michigan State University (MSU) [11]. A clear resonance peak was observed in the decay energy spectrum at $E = 150_{-150}^{+50}$ keV [11]. This has been confirmed by the GSI-LAND group, who reported the upper limit of the decay energy to be 40 and 120 keV with the confident level of 68% and 95%, respectively [12]. These experimental data on the ground state decay of ^{26}O have been theoretically analyzed in Refs. [18–21].

Very recently, new experimental data on the decay of the $^{25,26}\text{O}$ nuclei came out from the radioactive ion beam factory (RIBF) at RIKEN, which have revised the previous data with much higher statistics [15]. The energy of the ground state of ^{26}O has now been determined with a higher precision to be 18 ± 3 (stat) ± 4 (sys) keV [15].

Moreover, Ref. [15] has also reported a clear second peak at $1.28_{-0.08}^{+0.11}$ MeV [15], which is likely due to the excited 2^+ state. The data for the ^{25}O have also been revised in this experiment. While the previous measurements reported the $d_{3/2}$ resonance state at 770_{-10}^{+20} keV with the width of 172 ± 30 keV [31], and at 725_{-29}^{+54} keV with the width of 20_{-20}^{+60} keV [12], the new measurement has shown the $d_{3/2}$ resonance state at 749 (10) keV with the width of 88 (6) keV [15].

In this paper, we study the ground and excited resonance states in ^{26}O with a three-body model by taking into account the coupling to the continuum. The main aim of our study is to extract the di-neutron correlations and a halo nature of the ground state of ^{26}O from the two-neutron decay spectrum with updated empirical inputs for the model Hamiltonian. In the present $^{24}\text{O}+n+n$ three-body model, the neutron-core potential as well as the strength of the pairing interaction between the valence neutrons are calibrated by the empirical data. To this end, we adopt the new experimental data of Ref. [15] and refine the calculations performed in Refs. [20, 21]. With the same model input, we also discuss the structure of excited 0^+ and 2^+ resonance states, which were not presented in our previous publications.

The paper is organized as follows. In Sec. II, we discuss the resonance structure of the ^{25}O nucleus. We use the new experimental data for this nucleus to determine the n - ^{24}O potential and obtain the resonance states of ^{25}O . We also discuss how the Green's function can be used to estimate the width of the resonance states. In Sec. III, we discuss the decay energy spectrum for the 0^+ configuration of the ^{26}O nucleus. We also apply the bound state approximation and discuss the radius and the angular momentum configurations. In Sec. IV, we discuss the first 2^+ state, and make a comparison with other theoretical calculations. In Sec. V, we discuss the

angular correlation of the emitted two neutrons and show that the back-to-back emission is enhanced due to the dineutron correlation. We then summarize the paper in Sec. VI.

II. RESONANCE STRUCTURE OF THE ^{25}O NUCLEUS

A. Calibration of the n - ^{24}O potential and single-particle resonances

An important input for the three-body calculation is the potential between a neutron and the core nucleus. In order to calibrate it, we first discuss the properties of the two-body subsystem of ^{26}O , that is, the ^{25}O nucleus, using the neutron + ^{24}O model.

Assuming that ^{24}O is inert in the ground state, we consider the following single-particle Hamiltonian for the relative motion between a neutron and the core nucleus:

$$h_{nC} = -\frac{\hbar^2}{2\mu}\nabla^2 + V_{nC}(r), \quad (1)$$

where $\mu = A_c m_N / (A_c + 1)$ is the reduced mass, m_N and $A_c = 24$ being the nucleon mass and the mass number of the core nucleus, respectively. We employ the Woods-Saxon potential for the neutron-core potential,

$$V_{nC}(r) = \left(V_0 + V_{ls}(\mathbf{l} \cdot \mathbf{s}) \frac{1}{r} \frac{d}{dr} \right) \left[1 + \exp\left(\frac{r-R}{a} \right) \right]^{-1}, \quad (2)$$

where $R = r_0 A_c^{1/3}$. We use the same value for the diffuseness parameter, a , and the radius parameter, r_0 , as in Ref. [20], that is, $a=0.72$ fm and $r_0=1.25$ fm. With these values of a and r_0 , the depth parameter, V_0 , is determined to be -44.1 MeV in order to reproduce the energy of the $2s_{1/2}$ state, $\epsilon_{2s_{1/2}} = -4.09(13)$ MeV [31]. For the strength of the spin-orbit potential, V_{ls} , we use the new data for the energy of the unbound $d_{3/2}$ state, that is, $\epsilon_{d_{3/2}} = 749(10)$ keV [15]. To this end, we seek a Gamow resonance state by imposing the outgoing boundary condition to the radial wave function. The resultant value is $V_{ls} = 45.605$ MeV fm², which is slightly smaller than the value employed in Ref. [20]. This potential yields the resonance width of 87.2 keV, which agrees well with the experimental value, 86 (6) keV [15].

In addition to the $d_{3/2}$ resonance, we also find a broad $p_{3/2}$ and a relatively narrow $f_{7/2}$ resonances with this potential. For the $p_{3/2}$ resonance, the resonance energy and the width are $E = 0.577$ MeV and $\Gamma = 1.63$ MeV, respectively, while they are $E = 2.44$ MeV and $\Gamma = 0.21$ MeV for the $f_{7/2}$ resonance. Notice that, due to the lower centrifugal barrier, the $p_{3/2}$ resonance appears at a lower energy with a larger width compared to the $d_{3/2}$ and $f_{7/2}$ resonances. The existence of the three resonance states in ^{25}O is consistent with a prediction reported in Ref. [32] based on shell model and Skyrme Hartree-Fock calculations, although the resonance widths are not evaluated

TABLE I: Single-particle resonance states of the ^{25}O nucleus obtained with a n - ^{24}O model. The Woods-Saxon potential is calibrated using the energy of the $d_{3/2}$ resonance. The resonance energy, E , and the width, Γ , are obtained by imposing the outgoing wave boundary condition to the radial wave function for each angular momentum j and l .

angular momentum	E (MeV)	Γ (MeV)
$d_{3/2}$	0.749 (input)	0.0872
$p_{3/2}$	0.577	1.63
$f_{7/2}$	2.44	0.21
expt. $d_{3/2}$ [15]	0.749 (10)	0.088 (6)

there (see Table III and Fig. 12 in Ref. [32]). The energy and the width of each of these three resonance states are summarized in Table I. In Sec. III, we will discuss the structure of excited 0^+ states of ^{26}O in connection to these single-particle resonance states of ^{25}O .

B. One-particle Green's function and the resonance width

While we investigated in the previous subsection the resonance structure of the ^{25}O nucleus using the Gamow states with complex eigen-energies, the resonance structure can also be studied using the Green's function keeping the energy to be real. In this approach, the decay energy spectrum is given by

$$\frac{dP}{dE} = |\langle \Phi_{\text{ref}} | \psi_E \rangle|^2, \quad (3)$$

where Φ_{ref} is the wave function for a reference state. ψ_E is a continuum wave function at E for a Hamiltonian of interest and is given by

$$\psi_E(\mathbf{r}) = \frac{u_{jl}(r)}{r} \mathcal{Y}_{jlm}(\hat{\mathbf{r}}), \quad (4)$$

with

$$u_{jl}(r) \rightarrow \sqrt{\frac{2\mu}{\pi k \hbar^2}} \sin\left(kr - \frac{l}{2}\pi + \delta_{jl}(E) \right) \quad (r \rightarrow \infty). \quad (5)$$

Here, $\mathcal{Y}_{jlm}(\hat{\mathbf{r}})$ is the spin-angular wave function, $k = \sqrt{2\mu E}/\hbar$ is the wave number, and $\delta_{jl}(E)$ is the phase shift. The normalization factor in Eq. (5) is chosen such that the wave function ψ_E satisfies the normalization condition of $\int dE |\psi_E\rangle \langle \psi_E| = 1$. Equation (3) indicates that the decay energy spectrum dP/dE increases when the overlap between the reference state and the continuum state is large. Therefore, if one chooses the reference wave function to be well confined inside a barrier, the decay energy spectrum shows a peak around the resonance energy, at which there is an appreciable component of the continuum wave function inside the barrier. The reference state is referred to as a doorway state in Ref. [33].

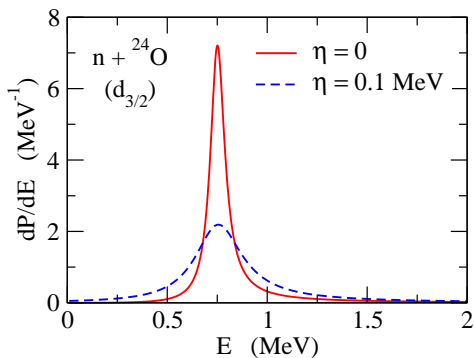


FIG. 1: (Color online) The decay energy spectrum for the $d_{3/2}$ configuration for the $n+^{24}\text{O}$ system. The solid line is obtained with Eq. (3) while the dashed line is obtained using Eq. (8) with a finite value of $\eta = 0.1$ MeV. The reference state Φ_{ref} is taken to be a bound neutron $d_{3/2}$ state in the ^{25}F nucleus.

The decay spectrum, Eq. (3), can also be expressed in a different way using the relation

$$\lim_{\eta \rightarrow 0} \frac{1}{x - i\eta} = \frac{1}{x} + i\pi\delta(x). \quad (6)$$

That is,

$$\frac{dP}{dE} = \int dE' |\langle \Phi_{\text{ref}} | \psi_{E'} \rangle|^2 \delta(E' - E), \quad (7)$$

$$= \frac{1}{\pi} \text{Im} \int dE' |\langle \Phi_{\text{ref}} | \psi_{E'} \rangle|^2 \frac{1}{E' - E - i\eta}, \quad (8)$$

where Im denotes the imaginary part and η is taken to be an infinitesimal number. Notice that

$$\int dE' |\psi_{E'} \rangle \frac{1}{E' - E - i\eta} \langle \psi_{E'} | = \frac{1}{\hbar - E - i\eta} \quad (9)$$

is nothing but the Green's function, $G(E)$. Equation (8) can therefore be written also as

$$\frac{dP}{dE} = \frac{1}{\pi} \text{Im} \langle \Phi_{\text{ref}} | G(E) | \Phi_{\text{ref}} \rangle. \quad (10)$$

The solid line in Fig. 1 shows the decay energy spectrum for the $d_{3/2}$ configuration of the ^{25}O nucleus. To draw this curve, we use the neutron $1d_{3/2}$ state at $\epsilon_{1d_{3/2}} = -0.811$ MeV in the ^{26}F nucleus for the reference state, Φ_{ref} . To this end, we use a similar potential as V_{nC} for the ^{25}O nucleus, but by modifying the strength of the spin-orbit potential to be $V_{ls} = 33.50$ MeV fm^2 taking into account the tensor force between the valence proton and neutron [30, 34–37]. As is expected, the decay energy spectrum shows a sharp peak at $E = 0.75$ MeV. The curve is approximately given by the Breit-Wigner function with a natural width of 0.087 MeV, which is consistent with the one obtained with the Gamow state method shown in the previous subsection (see Table I).

The dashed line in Fig. 1, on the other hand, is obtained with Eq. (8) by keeping a finite value of $\eta = 0.1$

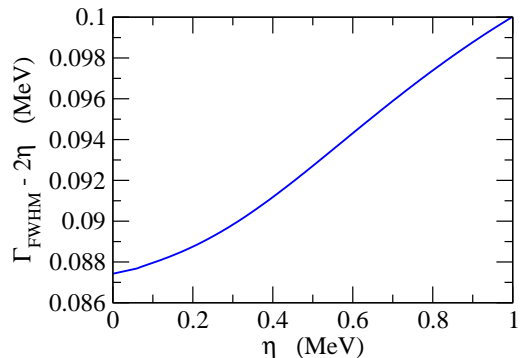


FIG. 2: (Color online) The $d_{3/2}$ resonance width for the $n+^{24}\text{O}$ system estimated from the decay energy spectrum with a finite value of η in the Green's function.

MeV. One can see that the peak position remains almost the same as in the solid line, but the width increases significantly because of the smearing factor $1/(E' - E - i\eta)$ in Eq. (8). If one approximates the decay energy spectrum in the limit of $\eta \rightarrow 0$ by the Breit-Wigner function with the resonance energy E_R and the natural width Γ , that is,

$$|\langle \Phi_{\text{ref}} | \psi_E \rangle|^2 \sim \frac{1}{2\pi} \frac{\Gamma}{(E - E_R)^2 + \frac{\Gamma^2}{4}}, \quad (11)$$

Eq. (8) is written as

$$\frac{dP}{dE} \sim \int dE' \frac{\frac{\Gamma}{2\pi}}{(E' - E_R)^2 + \frac{\Gamma^2}{4}} \cdot \frac{\frac{\eta}{\pi}}{(E - E')^2 + \eta^2}. \quad (12)$$

It is known that a convolution of the Breit-Wigner function with another Breit-Wigner function is again a Breit-Wigner function with the same resonance energy and the sum of the two resonance widths (this can be easily confirmed by performing the Fourier transform and then the inverse Fourier transform back to the original function). This equation thus becomes,

$$\frac{dP}{dE} \sim \frac{\frac{\Gamma+2\eta}{2\pi}}{(E - E_R)^2 + \frac{(\Gamma+2\eta)^2}{4}}. \quad (13)$$

This implies that the resonance width can numerically be estimated with the decay energy spectrum calculated with a finite value of η as

$$\Gamma = \Gamma_{\text{FWHM}} - 2\eta, \quad (14)$$

where Γ_{FWHM} is the full width at half maximum (FWHM) of the calculated spectrum, Eq. (8).

In order to test this idea, Fig. 2 shows the right hand side of Eq. (14) as a function of η . One can see that this method yields the resonance width within the accuracy of about 1% at $\eta = 0.1$ MeV. In practice, one may extrapolate the values for different η down to $\eta = 0$ in order to estimate the resonance width. This method is convenient particularly for the three-body problem which we shall discuss in the next section.

III. DECAY ENERGY SPECTRUM FOR 0^+ STATES OF THE ^{26}O NUCLEUS

A. Decay energy spectrum

Let us now solve a three-body Hamiltonian for the ^{26}O nucleus based on the $^{24}\text{O} + n + n$ model and discuss the decay dynamics. To this end, we consider the following three-body Hamiltonian,

$$H = h_{nC}(1) + h_{nC}(2) + v(\mathbf{r}_1, \mathbf{r}_2), \quad (15)$$

where h_{nC} is the single-particle Hamiltonian given by Eq. (1) and the pairing interaction is taken to be a density dependent contact interaction as [26, 27, 38–41],

$$v(\mathbf{r}_1, \mathbf{r}_2) = \delta(\mathbf{r}_1 - \mathbf{r}_2) \left(v_0 + \frac{v_\rho}{1 + \exp[(r_1 - R_\rho)/a_\rho]} \right). \quad (16)$$

For simplicity, we have neglected the two-body part of the recoil kinetic energy of the core nucleus, as in our previous works [20, 21]. In the density dependent pairing interaction, Eq. (16), the strength of the density independent part is given as [39],

$$v_0 = 2\pi^2 \frac{\hbar^2}{m_N} \frac{2a_{nn}}{\pi - 2k_C a_{nn}}, \quad (17)$$

where a_{nn} is the scattering length for the nn scattering and k_C is related to the cut-off energy, E_{cut} , as $k_C = \sqrt{m_N E_{\text{cut}}/\hbar^2}$. Following Ref. [39], we take $a_{nn} = -15$ fm. With $E_{\text{cut}} = 30$ MeV, this leads to $v_0 = -857.2$ MeV fm³. For the parameters for the density dependent part in Eq. (16), we determine them so as to reproduce the ground state energy of ^{26}O , $E = 18$ keV [15]. The values of the parameters which we employ are $R_\rho = 1.34 \times A_c^{1/3}$ fm, $a_\rho = 0.72$ fm, and $v_\rho = 928.95$ MeV fm³.

As in the previous section, the decay energy spectrum is obtained with the Green's method, Eq. (10), with some three-body wave function for Φ_{ref} and the two-particle Green's function given by $G(E) = 1/(H - E - i\eta)$. We evaluate the correlated Green's function, $G(E)$, using the relation [40],

$$G(E) = G_0(E) - G_0(E)v(1 + G_0(E)v)^{-1}G_0(E), \quad (18)$$

where the uncorrelated two-particle Green's function, $G_0(E)$, is given by

$$\begin{aligned} G_0(E) &= \frac{1}{h_{nC}(1) + h_{nC}(2) - E - i\eta}, \quad (19) \\ &= \sum_{j_1, l_1} \sum_{j_2, l_2} \int d\mathbf{e}_1 d\mathbf{e}_2 \frac{|\langle [\psi_1 \psi_2]^{(0^+)} \rangle \langle [\psi_1 \psi_2]^{(0^+)} |}{e_1 + e_2 - E - i\eta}. \end{aligned} \quad (20)$$

Since the interaction v is zero-ranged, the inversion of the operator $(1 + G_0(E)v)$ in Eq. (18) is best performed in the coordinate space on a finite radial grid [38, 40].

With Eqs. (18) and (20), the uncorrelated spectrum is then given by

$$\begin{aligned} \frac{dP_0}{dE} &= \frac{1}{\pi} \text{Im} \langle \Phi_{\text{ref}} | G_0(E) | \Phi_{\text{ref}} \rangle, \quad (21) \\ &= \frac{1}{\pi} \text{Im} \sum_{j_1, l_1} \sum_{j_2, l_2} \int d\mathbf{e}_1 d\mathbf{e}_2 \frac{|\langle \Phi_{\text{ref}} | [\psi_1 \psi_2]^{(0^+)} \rangle|^2}{e_1 + e_2 - E - i\eta}, \end{aligned} \quad (22)$$

while the correlated spectrum is evaluated as [40],

$$\begin{aligned} \frac{dP}{dE} &= \frac{dP_0}{dE} - \frac{1}{\pi} \text{Im} \int d\mathbf{r} d\mathbf{r}' \tilde{G}_D(\mathbf{r}) v(\mathbf{r}) \\ &\quad \times (1 + G_0(E)v)_{\mathbf{r}\mathbf{r}'}^{-1} G_D(\mathbf{r}'), \end{aligned} \quad (23)$$

with

$$\begin{aligned} G_D(\mathbf{r}) &= \sum_{j_1, l_1} \sum_{j_2, l_2} \int d\mathbf{e}_1 d\mathbf{e}_2 \\ &\quad \times \frac{\langle \mathbf{r}\mathbf{r}' | [\psi_1 \psi_2]^{(0^+)} \rangle \langle [\psi_1 \psi_2]^{(0^+)} | \Phi_{\text{ref}} \rangle}{e_1 + e_2 - E - i\eta}, \end{aligned} \quad (24)$$

and

$$\begin{aligned} \tilde{G}_D(\mathbf{r}) &= \sum_{j_1, l_1} \sum_{j_2, l_2} \int d\mathbf{e}_1 d\mathbf{e}_2 \\ &\quad \times \frac{\langle \Phi_{\text{ref}} | [\psi_1 \psi_2]^{(0^+)} \rangle \langle [\psi_1 \psi_2]^{(0^+)} | \mathbf{r}\mathbf{r}' \rangle}{e_1 + e_2 - E - i\eta}. \end{aligned} \quad (25)$$

Notice that $\tilde{G}_D(\mathbf{r})$ is not identical to $G_D^\dagger(\mathbf{r})$.

The upper panel of Fig. 3 shows the uncorrelated (the dashed line) and the correlated (the solid line) decay spectra for ^{26}O . To this end, we use the uncorrelated two-neutron state of ^{27}F with the $[[1d_{3/2}1d_{3/2}]^{(0^+)})$ configuration for the reference state Φ_{ref} , since the ^{26}O nucleus was produced in the single proton-knockout reaction from a secondary ^{27}F beam in the experiments of Refs. [11, 12, 15]. For a presentation purpose, we keep a finite value of $\eta = 0.1$ MeV in Eq. (20) in order to evaluate the uncorrelated Green's function. In fact, numerically it is much easier to evaluate the correlated Green's function with a finite value of η , especially when a natural width is small, since in any case one must discretize the energies in the quadratures in Eq. (20). In the figure, the main feature of the decay energy spectra is the same as that in Ref. [20]. That is, a peak appears at twice the single-particle resonance energy, 1.498 MeV, in the uncorrelated spectrum, which is largely shifted towards the threshold energy in the correlated spectrum due to the pairing correlation.

The lower panel of Fig. 3 shows the dependence of the result on the choice of the reference state. The solid line is the same as that in the upper panel, while the dot-dashed line is obtained with the correlated three-body wave function for the ^{27}F nucleus obtained with the $^{25}\text{F} + n + n$ model using the same pairing interaction as in Eq.

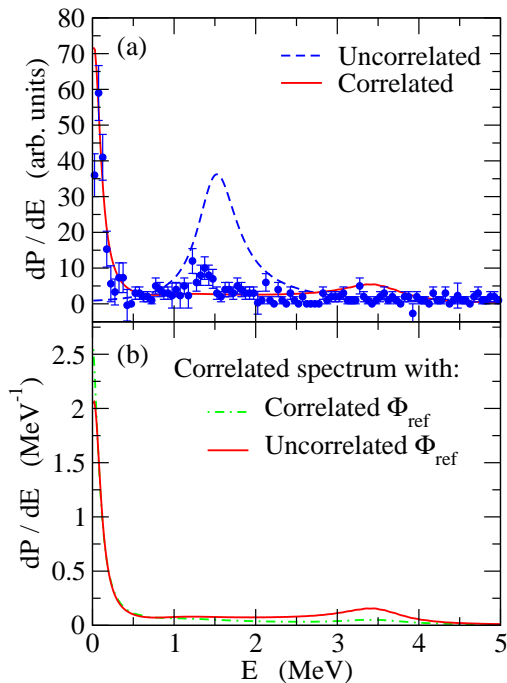


FIG. 3: (Color online) Upper panel: the uncorrelated (the dashed line) and the correlated (the solid line) decay energy spectra for the ^{26}O nucleus. The uncorrelated two-neutron state in ^{27}F with the $[[1d_{3/2}1d_{3/2}]^{(0^+)})$ configuration is employed for the reference state, Φ_{ref} . For a presentation purpose, a finite value of $\eta = 0.1$ MeV is used. The experimental data are taken from Ref. [15]. Lower panel: the dependence of the correlated decay spectrum on the choice of the reference state. The solid line is the same as that in the upper panel and is obtained with the uncorrelated two-particle wave function of ^{27}F . The dot-dashed line, on the other hand, is obtained with the correlated two-particle wave function of ^{27}F based on the $^{25}\text{F} + n + n$ three-body model.

(16). One can see that qualitatively the spectrum does not depend much on the choice of the reference state. In particular, the sharp low-energy peak is produced in both the calculations, although the height is somewhat lower in the calculation with the uncorrelated reference state. This is because the ground state is mainly composed of the $[[1d_{3/2}1d_{3/2}]^{(0^+)})$ configuration both in the ^{26}O and in the ^{27}F nuclei (see the next subsection).

This finding implies that the decay energy spectrum does not depend much on how the ^{26}O nucleus is produced. Intuitively, for a narrow resonance with a long lifetime, a nucleus loses its memory of how it was produced, before it decays under the barrier [42]. In this situation, the decay dynamics predominantly reflects properties of the continuum wave function of the final three-body system, Ψ_E . In the terminology of nuclear reaction, the decay involves only the final state interactions. This is in fact a good point of narrow resonances, since one does not have to bother with the reaction dynamics and/or the structure of the initial nucleus in analyzing observables in the decay process. We will discuss an

TABLE II: Ground state properties of the ^{26}O nucleus obtained with the bound state approximation with a box size of $R_{\text{box}} = 40$ fm. $\langle r_{nn}^2 \rangle$ and $\langle r_{c-2n}^2 \rangle$ are the mean-square neutron-neutron distance and the core-dineutron distance, respectively. The fractions of the main components and the spin-singlet component are also shown.

$\langle r_{nn}^2 \rangle$ (fm ²)	$\langle r_{c-2n}^2 \rangle$ (fm ²)	$[d_{3/2}]^2$ (%)	$[f_{7/2}]^2$ (%)	$[p_{3/2}]^2$ (%)	$[p_{1/2}]^2$ (%)	$[g_{9/2}]^2$ (%)	$S = 0$ (%)
40.2	18.5	66.1	18.3	10.5	1.50	1.15	54.8

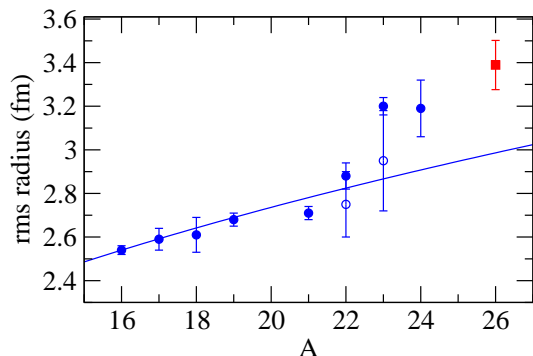


FIG. 4: (Color online) The root-mean-square (rms) radii of the oxygen isotopes as a function of the mass number A . The filled and open circles are the experimental data taken from Refs. [43] and [44], respectively. The filled square is the radius of the ^{26}O estimated with the three-body model calculation with the empirical rms radius of ^{24}O . The solid line shows a function $\sqrt{\langle r^2 \rangle} = r_0 A^{1/3}$ with $r_0 = 1.0$ fm, in which the value of r_0 is determined with the radius of ^{16}O .

example of this point in Sec. IV, that is, the angular correlation of the two emitted neutrons, which reflects the dineutron correlation in the continuum state of ^{26}O , rather than the properties of the initial state of ^{27}F .

In the following calculations, for simplicity, we shall use the uncorrelated wave function for the reference state Φ_{ref} .

B. Di-neutron correlation in the ground state

Since the resonance width is considerably small for the ground state of ^{26}O [10, 18], one would expect that a bound state approximation provides a reasonable result in discussing the ground state properties of the ^{26}O nucleus. Let us therefore obtain the ground state wave function by putting the ^{26}O nucleus in a large box as in Ref. [26]. To this end, we use the box size of $R_{\text{box}} = 40$ fm. Since the continuum states are treated approximately in this calculation, we slightly readjust the v_ρ parameter in the pairing interaction, Eq. (16), so that the resultant ground state energy is 18 keV.

Table II summarizes the properties of the ground state wave function thus obtained. One can see that the ground state wave function mainly consists of the $(d_{3/2})^2$

configuration, but there is also an appreciable admixture of other components, such as the $(f_{7/2})^2$ and the $(p_{3/2})^2$ components (see also Ref.[32]). From the calculated root-mean-square (rms) inter-neutron distance, $\sqrt{\langle r_{nn}^2 \rangle}$, and the core-dineutron distance, $\sqrt{\langle r_{c-2n}^2 \rangle}$, one can estimate the radius of the ^{26}O as [41],

$$\langle r^2 \rangle_{^{26}\text{O}} = \frac{24}{26} \langle r^2 \rangle_{^{24}\text{O}} + \delta \langle r^2 \rangle, \quad (26)$$

with

$$\delta \langle r^2 \rangle = \frac{1}{26} \left(\frac{2 \times 24}{26} \langle r_{c-2n}^2 \rangle + \frac{1}{2} \langle r_{nn}^2 \rangle \right). \quad (27)$$

Using the empirical rms radius of ^{24}O , $\sqrt{\langle r^2 \rangle_{^{24}\text{O}}} = 3.19 \pm 0.13$ fm [43], obtained with the interaction cross section measurement, we estimate the rms radius of ^{26}O to be $\sqrt{\langle r^2 \rangle_{^{26}\text{O}}} = 3.39 \pm 0.11$ fm. The radii of the oxygen isotopes are shown in Fig. 4. The filled and open circles are the experimental radii taken from Refs. [43] and [44], respectively, while the filled square is the calculated radius for ^{26}O . One can see that the radius of the ^{26}O nucleus is significantly larger than the empirical law of $r \propto A^{1/3}$, as is shown by the solid line in the figure. This may suggest a halo structure of the ^{26}O nucleus.

In order to see whether ^{26}O has a halo structure, Fig. 5 shows the density distribution of the ^{26}O nucleus. To this end, we construct the density of the core nucleus, ^{24}O , with the Skyrme-Hartree-Fock calculation with SLy4 interaction [45]. We do not take into account the pairing correlation in ^{24}O in order to be consistent with the three-body model for ^{26}O . This calculation yields 3.05 fm for the matter radius of ^{24}O , which agrees with the experimental value within the error bar. The upper and the lower panels in the figure show the density distribution in linear and logarithmic scales, respectively. One can see that the neutron distribution (the solid line) is more extended than the proton density (the dashed line) and than the neutron density in the core nucleus (the dotted line).

Figs. 6 and 7 show the two-particle density, $\rho(r_1, r_2, \theta_{12})$, of the ^{26}O nucleus with and without the weight factor of $8\pi^2 r^4 \sin \theta_{12}$, respectively. These are plotted as a function of $r_1 = r_2 = r$ and the angle between the valence neutrons, θ_{12} . One can see, especially in Fig. 7, that the two-particle density is well concentrated in the small θ_{12} , which is a clear manifestation of the dineutron correlation [26]. Notice that, with the Woods-Saxon potential which we employ, the position of the centrifugal barrier is at $r = 6.08$ fm for $d_{3/2}$. The dineutron correlation is thus present inside the barrier, hence before the two-neutron decay. The angular density defined by [26],

$$\rho(\theta_{12}) = 4\pi \int_0^\infty r_1^2 dr_1 \int_0^\infty r_2^2 dr_2 \rho(r_1, r_2, \theta_{12}), \quad (28)$$

is plotted in Fig. 8 as a function of θ_{12} . The figure also shows a decomposition into the spin-singlet ($S = 0$) and

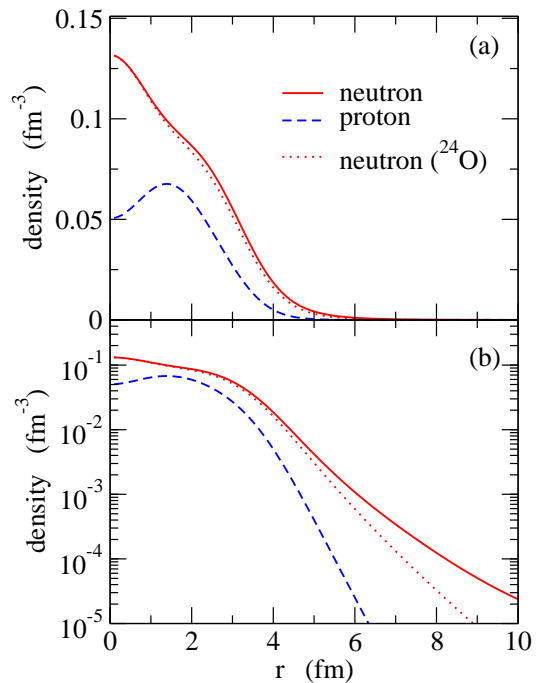


FIG. 5: (Color online) The density distribution of the ^{26}O nucleus in the linear (the upper panel) and in the logarithmic (the lower panel) scales, respectively. The solid and the dashed lines denote the neutron and the proton densities, respectively, while the dotted line shows the neutron density of the core nucleus, ^{24}O . The density distribution for the valence neutrons is obtained with the three-body model while the density of the core nucleus is constructed using the Skyrme-Hartree-Fock calculation.

and the spin-triplet ($S = 1$) components [38]. One can see that the dineutron component in the small θ_{12} region consists predominantly of the $S = 0$ component, while the peak in the large θ_{12} region mainly consists of the $S = 1$ component. This has some similarity to the ^{11}Li nucleus shown in Ref. [26], although the middle peak is absent in ^{11}Li due to the dominance of the $(p_{1/2})^2$ configuration instead of the $(d_{3/2})^2$ configuration.

In connection to the angular correlations of the two emitted neutrons, which we will discuss in Sec. V, it is interesting here to discuss the ground state density in the momentum space. Suppose that one expresses the ground state wave function in the coordinate space as [26, 38, 39]

$$\Psi(\mathbf{r}_1, \mathbf{r}_2) = \sum_{n, n'} \sum_{l, j} \alpha_{nn'lj} \Psi_{nn'lj}(\mathbf{r}_1, \mathbf{r}_2), \quad (29)$$

with

$$\Psi_{nn'lj}(\mathbf{r}_1, \mathbf{r}_2) = \sum_m \langle jmj - m | 00 \rangle \psi_{njlm}(\mathbf{r}_1) \psi_{n'jl-m}(\mathbf{r}_2), \quad (30)$$

where n is the radial node and the single-particle wave function is given by

$$\psi_{njlm}(\mathbf{r}) = \phi_{njl}(r) \mathcal{Y}_{jlm}(\hat{\mathbf{r}}). \quad (31)$$

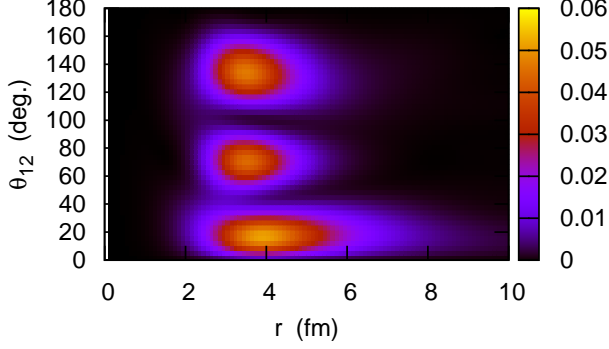


FIG. 6: (Color online) The two-particle density for the ^{26}O nucleus as a function of $r_1 = r_2 = r$ and the angle between the valence neutrons, θ_{12} . It is weighted with a factor of $8\pi^2 r^4 \sin \theta_{12}$.

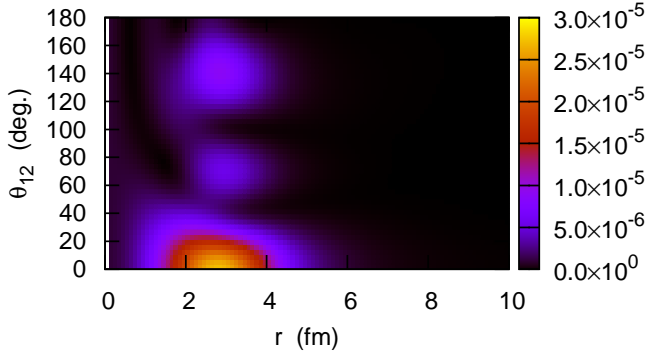


FIG. 7: (Color online) Same as Fig. 6, but without the weight factor of $8\pi^2 r^4 \sin \theta_{12}$.

Noticing that the Fourier transform of $\psi_{n_j l m}(\mathbf{r})$ is given by

$$\tilde{\psi}_{n_j l m}(\mathbf{k}) = \int d\mathbf{r} e^{i\mathbf{k}\cdot\mathbf{r}} \psi_{n_j l m}(\mathbf{r}) = i^l \tilde{\phi}_{n_j l}(k) \mathcal{Y}_{j l m}(\hat{\mathbf{k}}), \quad (32)$$

$$\equiv i^l \tilde{\psi}'_{n_j l m}(\mathbf{k}) \quad (33)$$

with

$$\tilde{\phi}_{n_j l}(k) = 4\pi \int r^2 dr j_l(kr) \phi_{n_j l}(r), \quad (34)$$

the Fourier transform of $\Psi(\mathbf{r}_1, \mathbf{r}_2)$ reads

$$\tilde{\Psi}(\mathbf{k}_1, \mathbf{k}_2) = \sum_{n, n'} \sum_{l, j} (-1)^l \alpha_{nn'lj} \tilde{\Psi}_{nn'lj}(\mathbf{k}_1, \mathbf{k}_2), \quad (35)$$

with

$$\tilde{\Psi}_{nn'lj}(\mathbf{k}_1, \mathbf{k}_2) = \sum_m \langle j m j - m | 00 \rangle \tilde{\psi}'_{n_j l m}(\mathbf{k}_1) \tilde{\psi}'_{n' j l - m}(\mathbf{k}_2). \quad (36)$$

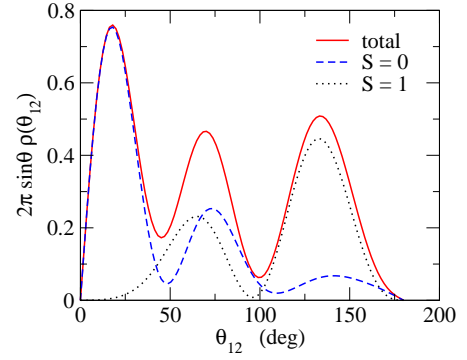


FIG. 8: (Color online) The angular density (weighted with a factor $2\pi \sin \theta_{12}$) for the ground state of the ^{26}O nucleus as a function of the angle between the two valence neutrons, θ_{12} . The solid line is for the total density, while the dashed and the dotted lines are for the spin-singlet ($S = 0$) and the spin-triplet ($S = 1$) components, respectively.

By comparing Eq. (29) with Eq. (35), one can notice that the role of odd-partial waves is opposite between the coordinate space and the momentum space. Notice that the dineutron correlation is caused by the coherent superposition between even- and odd- partial waves [28, 46, 47]. If the weight factors $\alpha_{nn'lj}$ in Eq. (29) are such that the wave function for $\mathbf{r}_1 = \mathbf{r}_2$ is enhanced and that for $\mathbf{r}_1 = -\mathbf{r}_2$ is suppressed, as in the dineutron correlation, the wave function in the momentum space therefore shows an enhancement for $\mathbf{k}_1 = -\mathbf{k}_2$ and a suppression for $\mathbf{k}_1 = \mathbf{k}_2$. This fact can also be understood in terms of the uncertainty relation between the space and the momentum.

The two-particle density in the momentum space, constructed with $\tilde{\Psi}(\mathbf{k}_1, \mathbf{k}_2)$, is shown in Fig. 9 as a function of $k_1 = k_2 = k$ and θ_{12} . One can clearly see that the two-particle density is indeed enhanced in the large θ_{12} region in the momentum space, reflecting the dineutron correlation shown in Fig. 6 in the coordinate space.

C. Excited 0^+ states

The decay energy spectrum shown in Fig. 3 shows that the ground energy peak does not vanish quickly and there is appreciable strength between $1 \leq E \leq 3$ MeV, indicating the presence of a few unresolved excited 0^+ resonances in this energy region. In addition, one can see a peak at 3.38 MeV. In order to better understand these structures, Fig. 10 shows the decay energy spectrum in a magnified way. One can see at least two peaks, the lower one at 1.22 MeV and the higher one at 3.38 MeV. For the higher energy peak, the width is estimated to be 0.737 MeV using the method discussed in Sec. II. On the other hand, for the lower energy peak, unfortunately the width cannot be estimated, because the resonance peak overlaps with other peaks and the full-width-at-half maximum cannot be defined.

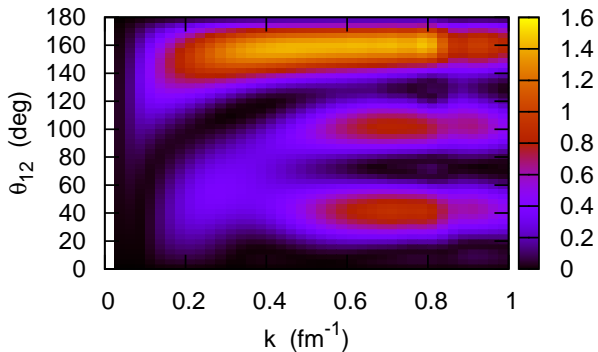


FIG. 9: (Color online) The two-particle density in the momentum space as a function of $k_1 = k_2 = k$ and the angle between the valence neutrons, θ_{12} . It is weighted with a factor of $8\pi^2 k^4 \sin \theta_{12}$.

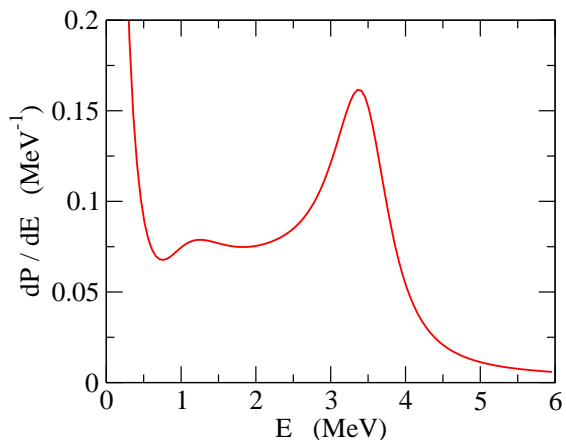


FIG. 10: (Color online) Same as Fig. 3, but plotted in a magnified way for the region of $E \geq 0.5$ MeV.

In order to understand the structure of these peaks, we evaluate the probabilities of angular momentum components in the wave functions. Since the correlated Green's function is expressed as

$$G(E) = \sum_{\widetilde{2p}} \frac{|\widetilde{2p}\rangle\langle\widetilde{2p}|}{E_{2p} - E - i\eta}, \quad (37)$$

where $|\widetilde{2p}\rangle$ is the correlated two-particle wave function at $E = E_{2p}$, the amplitude of the correlated wave function on an uncorrelated basis, $|2p\rangle$, can be extracted as

$$\langle\Phi_{\text{ref}}|\widetilde{2p}\rangle\langle\widetilde{2p}|2p\rangle = \text{Im}\langle\Phi_{\text{ref}}|G(E_{2p})|2p\rangle. \quad (38)$$

Notice that many continuum states are degenerate in energy at a given value of E_{2p} (this can be easily understood in the uncorrelated limit, in which there are many combinations of (e_1, e_2, j, l) leading to the 0^+ configuration with the same energy $E = e_1 + e_2$). By taking the

TABLE III: Properties of the ground and excited 0^+ states in ^{26}O corresponding to the three peaks in the decay energy spectrum. For the peak at $E = 3.38$ MeV, the resonance width is also evaluated using the method presented in Sec. II-B.

E (MeV)	Γ (MeV)	$(p_{3/2})^2$ (%)	$(d_{3/2})^2$ (%)	$(f_{7/2})^2$ (%)
0.018	-	10.5	66.1	18.3
1.22	-	60.3	26.8	2.02
3.38	0.737	10.4	24.9	62.1

overlap $\langle\Phi_{\text{ref}}|\widetilde{2p}\rangle$ in Eq. (38), only those correlated wave functions which have an appreciable overlap with the reference wave function, thus the resonance wave functions, contribute on the left hand side. Because of this property, when one extracts the amplitudes of resonance wave functions, we find that this method is more convenient than a similar method presented in Ref. [38], which uses the relation

$$\langle\Phi_{\text{ref}}|\delta(\mathbf{r}_1 - \mathbf{r}_2)|\widetilde{2p}\rangle\langle\widetilde{2p}|2p\rangle = \text{Im}\langle\Phi_{\text{ref}}|\delta(\mathbf{r}_1 - \mathbf{r}_2)G(E_{2p})|2p\rangle. \quad (39)$$

In practice, we use the uncorrelated basis $|2p\rangle$ obtained with the box discretization method (see the previous subsection) with a relatively small box size in order to eliminate the contribution outside the centrifugal barrier, and evaluate the amplitudes according to,

$$\langle\widetilde{2p}|2p\rangle = \frac{\text{Im}\langle\Phi_{\text{ref}}|G(E_{2p})|2p\rangle}{\sum_{2p} |\text{Im}\langle\Phi_{\text{ref}}|G(E_{2p})|2p\rangle|^2}, \quad (40)$$

even though the true continuum wave function is not square integrable.

The results obtained with $R_{\text{box}} = 15$ fm are summarized in Table III. The table also shows the result for the ground state obtained in the previous subsection with the box discretization method. One can see that these three resonance peaks nicely reflect the single-particle resonance states of the two-body subsystem, $n+^{24}\text{O}$, shown in Table I. That is, the first (i.e., the ground state), the second, and the third peaks in the decay energy spectrum mainly consist of the $(d_{3/2})^2$, $(p_{3/2})^2$, and $(f_{7/2})^2$ configurations, respectively, as is expected from the single-particle resonances.

In Ref. [19], Grigorenko and Zhukov obtained two excited 0^+ states at 1.7 and 2.6 MeV, in addition to the ground state resonance at 0.01 MeV. All these resonance states show the dominance of the $(d_{3/2})^2$ configurations, and thus their excited 0^+ states are apparently different from the resonance peaks found in the present calculation. As we have mentioned, unresolved resonances may exist around 2 MeV in the decay spectrum shown in Fig. 10, and the resonance states found by Grigorenko and Zhukov might correspond to some of these. As for the $(f_{7/2})^2$ resonance at 3.38 MeV, it is not clear whether they have included the $l = 3$ configuration in the $n-^{24}\text{O}$ channel, since they have mentioned the $n-^{24}\text{O}$ potential

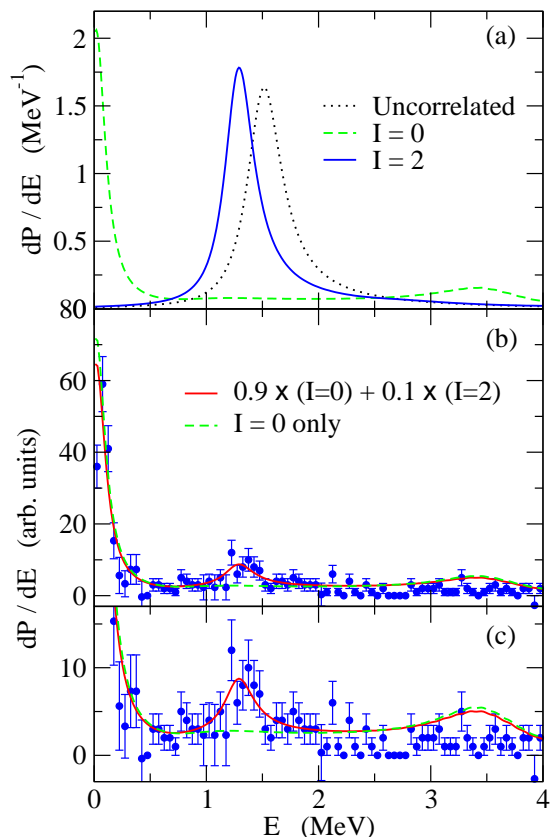


FIG. 11: (Color online) Top panel: The decay energy spectrum of the ^{26}O nucleus. The dashed and the solid lines are for the 0^+ and 2^+ states, respectively, while the dotted line shows the uncorrelated spectrum. Middle panel: The decay energy spectrum obtained by mixing the 0^+ and the 2^+ components, as is indicated in the figure. The experimental data are taken from Ref. [15]. Bottom panel: same as the middle panel, but with a larger scale.

only for the s , p , and d waves [19]. The correspondence is thus not certain at this moment.

IV. THE 2^+ STATE

Let us next discuss the first 2^+ state in ^{26}O . One of the most important findings in the recent experiment reported in Ref. [15] is a finding of a clear second peak at $E = 1.28^{+0.11}_{-0.08}$ MeV, which is likely attributed to the 2^+ state. A signal of this peak was weak in the earlier experiments, mainly because the statistics were not sufficient. In Ref. [21], we have investigated the 2^+ state in the ^{26}O nucleus using the three-body model. That is, the energy spectrum for this state can still be obtained with the Green's function approach, by using a 2^+ state for the reference state, Φ_{ref} , as well as in the unperturbed Green's function, Eq. (20) [21]. Here we repeat the same calculation, but with the revised set of input parameters. The results for the decay energy spectrum is shown in

TABLE IV: Comparison of the energies of the $3/2^+$ state of ^{25}O and the 2^+ state of ^{26}O obtained with several methods. These values, given in units of MeV, are measured from the thresholds.

method	^{25}O ($3/2^+$)	^{26}O (2^+)	Reference
Shell model (USDA)	1.301	2.4	[12, 49]
Shell model (USDB)	1.303	2.45	[12, 49]
chiral NN + 3N	0.742	1.64	[12]
continuum shell model	1.002	1.87	[50]
continuum-coupled shell model	0.86	1.66	[33]
3-body model	?	1.6	[19]
3-body model	0.749 (input)	1.282	this work
Experiment	0.749 (10)	$1.28^{+0.11}_{-0.08}$	[15]

Fig. 11. Again, the main feature remains the same as in Ref. [21]. That is, due to the pairing interaction between the valence neutrons, the energy of the 2^+ state is slightly shifted towards lower energies from the unperturbed energy, whereas the energy shift is much larger for the 0^+ state due to the larger overlap between the wave functions of the two neutrons. The 2^+ peak appears at 1.282 MeV, which agrees perfectly with the experimental data. The middle and the bottom panels of Fig. 11 show the energy spectrum obtained by mixing the 2^+ component by 10% to the 0^+ component. As has already been shown in Ref. [21], the experimental data are better reproduced by mixing the 2^+ component.

While we achieve an excellent agreement with the experimental data for the energy of the 2^+ state, it is striking to notice that most of theoretical calculations performed so far overestimate the energy. For instance, an ab-initio calculation with chiral NN and $3N$ interactions predicts E_{2^+} to be 1.6 MeV above the ground state [12] (see also Ref. [48]). Shell model calculations with the USDA and USDB interactions [49] yield the excitation energy of 1.9 and 2.1 MeV, respectively [12], whereas the continuum shell model calculations predict the 2^+ energy above the threshold to be 1.87 MeV [50] and 1.66 MeV [33]. The recent three-body model calculation by Grigorenko and Zhukov shows the energy to be 1.6 MeV [19]. We summarize these results in Table IV together with the energy of the $3/2^+$ state in ^{25}O for each calculation. It is not clear what causes these overestimates of the 2^+ energy, but the 2^+ state should certainly appear at an energy slightly lower than the unperturbed state, as long as the three-body structure is reasonable. In this sense, the ab-initio calculation with chiral NN and $3N$ interactions shows the opposite trend, and the shell model calculations, except for the continuum shell model calculations of Refs. [33, 50], seem to overestimate the correlation (unfortunately, we cannot judge this for the recent three-body model calculation of Grigorenko and Zhukov, because they do not discuss the energy of the ^{25}O nucleus and also because the exact form of the spin-orbit form which they employ is not clear).

TABLE V: Properties of the 2^+ state obtained with the present three-body model. The experimental value of the energy is $E_{\text{exp}} = 1.28_{-0.08}^{+0.11}$ MeV [15].

E	Γ	$(d_{3/2})^2$	$(p_{1/3}f_{7/2})$	$(f_{7/2})^2$
(MeV)	(MeV)	(%)	(%)	(%)
1.282	0.121	94.6	2.06	1.05

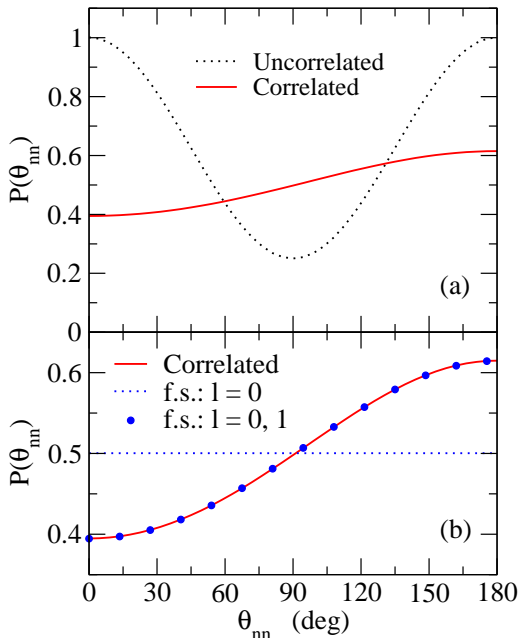


FIG. 12: (Color online) Upper panel: the angular correlations between the emitted neutrons from the two-neutron decay of ^{26}O . The solid and the dotted lines show the correlated and the uncorrelated distributions, respectively. Lower panel: the decomposition of the correlated distribution into the angular momentum components. The dotted line and the filled circles are obtained by including the angular momentum of the final state up to $l = 0$ and $l = 1$, respectively.

In addition to the energy of the 2^+ state, in this paper we also evaluate the width and the angular momentum components using the methods presented in the previous sections. The results are $\Gamma = 0.121$ MeV, and 94.6 % for the $(d_{3/2})^2$ configuration, 2.06 % for the $(p_{1/3}f_{7/2})$ configuration, and 1.05 % for the $(f_{7/2})^2$ configuration. These values are summarized in Table V. The 2^+ state is predominantly consists of the $(d_{3/2})^2$ configuration, which supports our three-body model argument of the energy of the 2^+ state [21].

V. ANGULAR CORRELATIONS

We next discuss the angular correlation of the emitted neutrons from the ground state of ^{26}O . The amplitude for emitting the two neutrons with spin components of

s_1 and s_2 and momenta \mathbf{k}_1 and \mathbf{k}_2 is given by [20, 40],

$$f_{s_1 s_2}(\mathbf{k}_1, \mathbf{k}_2) = \sum_{j,l} e^{-il\pi} e^{i(\delta_1 + \delta_2)} M_{j,l,k_1,k_2} \times \langle [\mathcal{Y}_{jl}(\hat{\mathbf{k}}_1) \mathcal{Y}_{jl}(\hat{\mathbf{k}}_2)]^{(00)} | \chi_{s_1} \chi_{s_2} \rangle, \quad (41)$$

where χ_s is the spin wave function and δ is the nuclear phase shift. M_{j,l,k_1,k_2} is the decay amplitude given by

$$M_{j,l,k_1,k_2} = \langle (jj)^{(00)} | (1 + vG_0)^{-1} | \Phi_{\text{ref}} \rangle \sqrt{\frac{de_1}{dk_1}} \sqrt{\frac{de_2}{dk_2}}, \quad (42)$$

in which the unperturbed Green's function, G_0 , is evaluated at $E = e_1 + e_2$. The angular distribution is then obtained as

$$P(\theta_{12}) = 4\pi \sum_{s_1, s_2} \int dk_1 dk_2 |f_{s_1 s_2}(k_1, \hat{\mathbf{k}}_1 = 0, k_2, \hat{\mathbf{k}}_2 = \theta_{12})|^2, \quad (43)$$

where we have set the z -axis to be parallel to \mathbf{k}_1 and evaluated the angular distribution as a function of the opening angle, θ_{12} , of the two emitted neutrons. As in Ref. [20], for simplicity, we compute the correlated distribution only at the peak energy of the spectrum and then normalize the calculated distribution.

The upper panel of Fig. 12 shows the angular distributions thus obtained. In the absence of the correlation between the valence neutrons, the angular distribution is symmetric with respect to $\theta_{12} = \pi/2$ (see the dotted line). On the other hand, in the presence of the interaction between the valence neutrons, the angular distribution becomes highly asymmetric, with an enhancement of the back-to-back emission [18, 20], as is shown by the solid line. This is a natural consequence of the dineutron correlation in the momentum space shown in Fig. 9.

As we have already discussed in Sec. II B, the dineutron correlation is caused by the interference between even- and odd- angular momentum configurations. In order to demonstrate this in connection to the angular correlation of the emitted neutrons, the lower panel of Fig. 12 shows the decomposition of the distribution into several angular momentum components. The dotted line is obtained by including only $l=0$ in Eq. (41), which leads to a flat distribution reflecting the property of the s -wave. The filled circles, on the other hand, are obtained by including both $l=0$ and $l=1$. One can now see the enhancement of the back-to-back emission, due to the interference between the $l=0$ and $l=1$ components, reflecting the dineutron correlation.

Moreover, one can also see that the angular distribution is almost exhausted only by the $l=0$ and $l=1$ components. One can view this as follows. That is, the original d^2 component in the reference wave function, Φ_{ref} , is scattered by the neutron-neutron interaction to the s^2 and p^2 configurations during the penetration of the centrifugal barrier, and are then observed as emitted neutrons from ^{26}O [18]. The operator $(1 + vG_0)^{-1} = 1 - vG_0 + vG_0 vG_0 - \dots$ in Eq. (42) has a responsibility

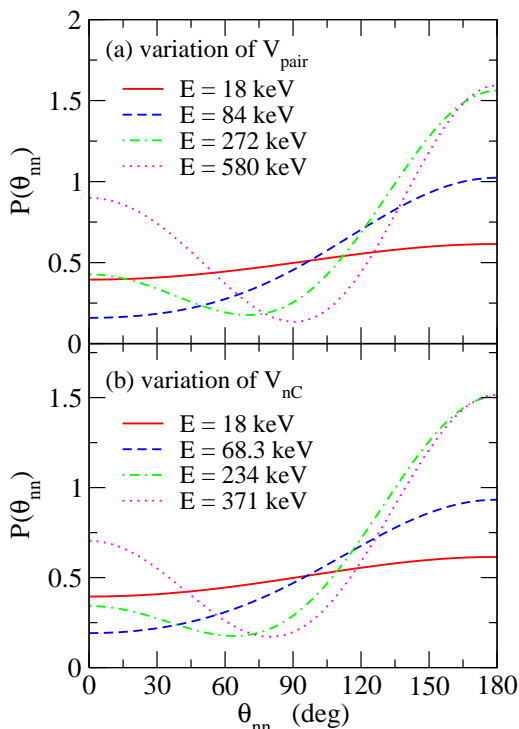


FIG. 13: (Color online) The dependence of the correlated angular distribution on the energy of the ground state. The upper panel is obtained by varying the energy by changing the pairing interaction between the two valence neutrons. On the other hand, the lower panel is obtained by shifting the resonance energy of the $d_{3/2}$ state in ^{25}O keeping the strength of the pairing interaction to be the same.

for this multiple scattering process during the penetration. The mixing between the s^2 and p^2 configurations is such that the back-to-back emission is enhanced being consistent with the dineutron correlation. In principle, the two neutrons may be scattered to high partial waves, but these are suppressed due to high centrifugal barriers.

As compared to the angular distribution reported in Ref. [20], the degree of asymmetry is smaller in the present calculation shown in Fig. 12. This is due to the smaller ground state energy, that is, we employ the ground state energy of 18 keV while Ref. [20] considered the energy of 140 keV. Since the energy is smaller, the p wave contribution is smaller in the present calculation. This leads to a smaller admixture between the s -wave and the p -wave components, and thus the smaller asymmetry in the angular distribution. In order to see this, Fig. 13 shows the dependence of the angular distribution on the ground state energy. For this purpose, we vary the ground state energy in two different ways. In the first calculations, we vary it by changing the strength of the pairing interaction, while we vary the $d_{3/2}$ resonance energy of the ^{25}O in the second calculation keeping the strength of the pairing interaction to be the same. In either way, one can see that the asymmetry indeed becomes larger as the ground state energy increases. If the

ground state energy further increases, the d -wave starts contributing, and the forward angle components grow up, even though the back-to-back emission is still enhanced due to the dineutron correlation.

Very recently, Kohley *et al.* extracted experimentally the three-body correlations from the ground state decay of ^{26}O [14]. The observed angular correlation has shown an enhancement of the forward angle emissions, in contradictory to Fig. 12. Kohley *et al.* have also performed the Monte Carlo simulations and have figured out that the observed three-body correlations are insensitive to the theoretical predictions [14]. That is, even a theoretical calculation with the enhancement of back-to-back emission leads to the opposite trend in the actual measurement, *i.e.*, the enhancement of forward angles. Kohley *et al.* argue that this is due to the uncertainty in the momentum of the ^{24}O nucleus at the reaction point in the target, which provides a large impact especially when the decay energy is small [14]. A confirmation of our prediction shown in Fig. 12 therefore seems quite challenging at this moment, and a further experimental development will still be necessary.

VI. SUMMARY

We have investigated the two-neutron emission decay of the unbound nucleus ^{26}O using the $^{24}\text{O} + n + n$ three-body model. To this end, we have calibrated the model parameters using the new experimental data measured at RIKEN. We have first discussed properties of the two-body subsystem, $^{25}\text{O} = ^{24}\text{O} + n$. Using a Woods-Saxon potential which reproduces the energy of the $d_{3/2}$ resonance, we have shown that the calculated width of the $d_{3/2}$ resonance as a Gamow state agrees well with the experimental data. In addition to the known $d_{3/2}$ resonance, we have also found a broad $p_{3/2}$ and a relatively narrow $f_{7/2}$ resonance states above the $d_{3/2}$ resonance. We have then calculated the decay energy spectrum of ^{26}O . The strength of the pairing interaction between the two valence neutrons was tuned in order to reproduce the ground state energy of the ^{26}O nucleus. We have shown that this interaction leads to an excellent agreement with the experimental data for the excited 2^+ state. We have also investigated the ground state properties employing the bound state approximation. We have shown that the density distribution shows a clear signature of dineutron correlation, with an extended distribution of the valence neutrons. We have found that the ground state of ^{26}O is dominated by the $(d_{3/2})^2$ configuration. In addition to the ground state, we have found at least two more excited 0^+ states, which consist mainly of the $(p_{3/2})^2$ and the $(f_{7/2})^2$ configurations, respectively, being consistent with the resonance structure of the two-body subsystem. For the $(f_{7/2})^2$ resonance, we have estimated also the resonance width. For the angular correlation of the two emitted neutrons, we have confirmed the result of our previous calculations, that is, an enhancement

of the back-to-back emission. We have argued that this enhancement of the back-to-back emission is a clear signature of dineutron correlation in ^{26}O , which can be understood in a simple term of uncertainty relation between the space and the momentum.

The unbound nucleus ^{26}O studied in this paper is a unique three-body system, which is unbound only slightly with an extremely small decay energy. This property would offer an interesting opportunity for further experimental and theoretical investigations on many-body correlations in neutron-rich nuclei. In this situation, the two-particle Green's function method will be a useful means in order to analyze experimental data. A theoretical challenge is to extend it to a four body decay,

such as ^{28}O . Another theoretical challenge is to apply it to the unbound ^{16}Be and ^{13}Li nuclei, both of which have been observed experimentally. To that end, a treatment of the deformation and the Borromean nature of the core nuclei would be crucial in the former and the latter unbound nuclei, respectively.

Acknowledgments

We thank Y. Kondo, T. Nakamura, W. Nazarewicz, and B.A. Brown for useful discussions.

-
- [1] M. Meister *et al.*, Phys. Rev. Lett. **91**, 162504 (2003).
 [2] M. Meister *et al.*, Nucl. Phys. **A723**, 13 (2003).
 [3] M.S. Golovkov *et al.*, Phys. Rev. Lett. **93**, 262501 (2004).
 [4] M.S. Golovkov *et al.*, Phys. Rev. **C72**, 064612 (2005).
 [5] H.T. Johansson *et al.*, Nucl. Phys. **A842**, 15 (2010).
 [6] H.T. Johansson *et al.*, Nucl. Phys. **A847**, 66 (2010).
 [7] S.I. Sidorchuk *et al.*, Phys. Rev. Lett. **108**, 202502 (2012).
 [8] Z. Kohley *et al.*, Phys. Rev. Lett. **109**, 232501 (2012).
 [9] A. Spyrou *et al.*, Phys. Rev. Lett. **108**, 102501 (2012).
 [10] Z. Kohley *et al.*, Phys. Rev. **C87**, 011304(R) (2013).
 [11] E. Lunderberg *et al.*, Phys. Rev. Lett. **108**, 142503 (21012).
 [12] C. Caesar *et al.*, Phys. Rev. **C88**, 034313 (2013).
 [13] Z. Kohley *et al.*, Phys. Rev. Lett. **110**, 152501 (2013).
 [14] Z. Kohley *et al.*, Phys. Rev. **C91**, 034323 (2015).
 [15] Y. Kondo *et al.*, Phys. Rev. Lett. **116**, 102503 (2016).
 [16] Yu. Aksyutina *et al.*, Phys. Lett. **B666**, 430 (2008).
 [17] L.V. Grigorenko, I.G. Mukha, C. Scheidenberger, and M.V. Zhukov, Phys. Rev. **C84**, 021303(R) (2011).
 [18] L.V. Grigorenko, I.G. Mukha, and M.V. Zhukov, Phys. Rev. Lett. **111**, 042501 (2013).
 [19] L.V. Grigorenko and M.V. Zhukov, Phys. Rev. **C91**, 064617 (2015).
 [20] K. Hagino and H. Sagawa, Phys. Rev. **C89**, 014331 (2014).
 [21] K. Hagino and H. Sagawa, Phys. Rev. **C90**, 027303 (2014).
 [22] Y. Kikuchi, T. Matsumoto, K. Minomo, and K. Ogata, Phys. Rev. **C88**, 021602 (2013).
 [23] M. Pfützner, M. Karny, L.V. Grigorenko, and K. Riisager, Rev. Mod. Phys. **84**, 567 (2012), and references therein.
 [24] M. Matsuo, K. Mizuyama, and Y. Serizawa, Phys. Rev. **C71**, 064326 (2005).
 [25] M. Matsuo, Phys. Rev. **C73**, 044309 (2006).
 [26] K. Hagino and H. Sagawa, Phys. Rev. **C72**, 044321 (2005).
 [27] H. Sagawa and K. Hagino, Euro. Phys. J. **A51**, 102 (2015).
 [28] N. Pillet, N. Sandulescu, and P. Schuck, Phys. Rev. **C76**, 024310 (2007).
 [29] H. Sakurai *et al.*, Phys. Lett. **B448**, 180 (1999).
 [30] T. Otsuka, T. Suzuki, J.D. Holt, A. Schwenk, and Y. Akaishi, Phys. Rev. Lett. **105**, 032501 (2010).
 [31] C.R. Hoffman *et al.*, Phys. Rev. Lett. **100**, 152502 (2008).
 [32] A. Lepailleur *et al.*, Phys. Rev. **C92**, 054309 (2015).
 [33] K. Tsukiyama, T. Otsuka, and R. Fujimoto, Prog. Theor. Exp. Phys. **2015**, 093D01 (2015).
 [34] T. Otsuka, T. Suzuki, R. Fujimoto, H. Grawe, and Y. Akaishi, Phys. Rev. Lett. **95**, 232502 (2005).
 [35] Fl. Stancu, D.M. Brink, and H. Flocard, Phys. Lett. **68B**, 108 (1977).
 [36] G. Colo, H. Sagawa, S. Fracasso, and P.F. Bortignon, Phys. Lett. **B646**, 227 (2007).
 [37] T. Lesinski *et al.*, Phys. Rev. **C76**, 014312 (2007).
 [38] G.F. Bertsch and H. Esbensen, Ann. Phys. (N.Y.) **209**, 327 (1991).
 [39] H. Esbensen, G.F. Bertsch, and K. Hencken, Phys. Rev. **C56**, 3054(1997).
 [40] H. Esbensen and G.F. Bertsch, Nucl. Phys. **A542**, 310 (1992).
 [41] N. Vinh Mau and J.C. Pacheco, Nucl. Phys. **A607**, 163 (1996).
 [42] L.V. Grigorenko, I.A. Egorova, R.J. Charity, and M.V. Zhukov, Phys. Rev. **C86**, 061602(R) (2012).
 [43] A. Ozawa *et al.*, Nucl. Phys. **A691**, 599 (2001).
 [44] R. Kanungo *et al.*, Phys. Rev. **C84**, 061304(R) (2011).
 [45] E. Chabanat, P. Bonche, P. Haensel, J. Meyer, and F. Schaeffer, Nucl. Phys. **A635**, 231 (1998).
 [46] F. Catara, A. Insolia, E. Maglione, and A. Vitturi, Phys. Rev. **C29**, 1091 (1984).
 [47] K. Hagino, A. Vitturi, F. Perez-Bernal, and H. Sagawa, J. Phys. **G38**, 015105 (2011).
 [48] H. Hergert, S. Binder, A. Calci, J. Langhammer, and R. Roth, Phys. Rev. Lett. **110**, 242501 (2013).
 [49] B.A. Brown and W.A. Richter, Phys. Rev. **C74**, 034315 (2006).
 [50] A. Volya and V. Zelevinsky, Phys. Rev. **C74**, 064314 (2006).